Mendeleev Commun., 2027, **37**, just accepted

Mendeleev Communications

26/8137

Received 03.07.26
Revised 15.10.26

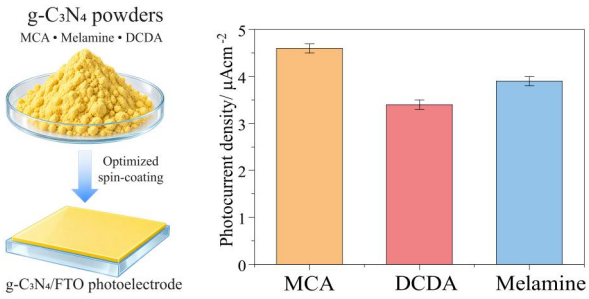
Supramolecular complex of melamine and cyanuric acid as a precursor for the graphitic carbon nitride (g-C_3N_4)-based photoelectrodes

Victoria A. Lomakina,[a] Angelina V. Zhurenok,[a] Dina V. Markovskaya,[a] Denis D. Mishchenko,[a,b] Svetlana V. Cherepanova[a] and Ekaterina A. Kozlova[a*]

[a] *Federal Research Center G. K. Boreskov Institute of Catalysis, Siberian Branch of the Russian Academy of Sciences, 630090 Novosibirsk, Russian Federation. E-mail: kozlova@catalysis.ru*
[b] *Synchrotron Radiation Facility 'SKIF', Boreskov Institute of Catalysis, Siberian Branch of the Russian Academy of Sciences, 630559 Koltsovo, Novosibirsk Region, Russian Federation*

DOI: 10.71267/mencom.8137

This work investigates the effects of precursor type and deposition method on the photoelectrochemical activity of g-C_3N_4 thin films, with spin-coating providing the highest photocurrent density among the investigated deposition techniques. Under optimized spin-coating conditions, the photoelectrode based on g-C_3N_4 synthesized from the supramolecular melamine–cyanuric acid complex exhibited a photocurrent density of 4.6 μA cm^{-2}, exceeding those of photoelectrodes based on melamine- and dicyandiamide-derived g-C_3N_4. The enhanced performance is consistent with more favorable charge transport and lower impedance.



Keywords: g-C_3N_4, photoelectrochemistry, spin-coating, thin-film photoelectrodes, EIS analysis.

Graphitic carbon nitride (g-C_3N_4) is a promising metal-free semiconductor for photocatalytic and photoelectrochemical applications owing to its ~2.7 eV band gap, high chemical and thermal stability and relatively simple synthesis.[1,2] Its performance strongly depends on morphology, defect structure, specific surface area and charge carrier separation and transport.[3-5] Machine learning studies have likewise identified precursor type, specific surface area and structure as important descriptors of g-C_3N_4 functionality and catalytic activity. These studies also suggest that homo- and heterojunction formation can enhance performance.[4–7] Precursor-dependent decomposition and polycondensation pathways produce materials with different morphologies, defect densities, degrees of condensation and electronic structures.[3,4,8] Although this effect is well established in photocatalysis,[3–5,9] its influence on photoelectrochemical performance remains less systematically studied and direct comparisons under identical conditions are scarce.[10,11] Photoelectrode fabrication also affects performance through film thickness and uniformity, agglomeration, adhesion and interparticle contacts, which control charge transport and recombination.[12,13]

In this work, g-C_3N_4 samples obtained from different precursors were compared under identical photoelectrochemical conditions using a common optimized electrode fabrication procedure.

Melamine (M), dicyandiamide (DCDA) and a supramolecular complex of melamine and cyanuric acid (MCA) were used as precursors. g-C_3N_4 (M) and g-C_3N_4 (DCDA) were obtained by calcination at 600 °C for 4 h, whereas g-C_3N_4 (MCA) was prepared at 550 °C for 1 h. These precursor-specific conditions were selected based on previous studies.[8,14,15] The comparison thus reflects both precursor identity and thermal history. Synthesis details are provided in the Online Supplementary

© Mendeleev Communications.

Materials. X-ray diffraction (XRD) patterns of all samples show the characteristic reflections near 13° and 27°, assigned to the (100) and (002) planes of g-C_3N_4, respectively (Figure 1(a)).[16,17]

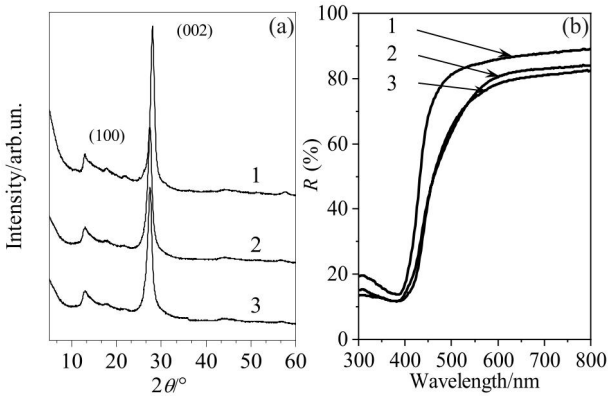


Figure 1 (a) XRD patterns: 1 - g-C_3N_4 (MCA), 2 - g-C_3N_4 (DCDA), 3 - g-C_3N_4 (M); (b) diffuse reflectance spectra: 1 - g-C_3N_4 (M), 2 - g-C_3N_4 (DCDA), 3 - g-C_3N_4 (MCA).

As shown in Table 1, the g-C_3N_4 (MCA) sample retains a similar in-plane crystallite size (L_a) but exhibits a larger crystallite size perpendicular to the layers L_c (9.5 vs 7.6 nm for DCDA) and the smallest interlayer spacing d_{002} (3.18 Å), indicating a more ordered and densely packed structure.

Table 1 Structural and physicochemical properties of the synthesized g-C_3N_4 samples

Sample	L_a/nm	L_c/nm	d_{002}/Å	d_{100}/Å	S_{BET}/m^2·g^{-1}	E_g/eV
g-C_3N_4 (DCDA)	5.1	7.6	3.24	6.73	22.6	2.6
g-C_3N_4 (M)	5.0	8.9	3.23	6.70	27.9	2.65
g-C_3N_4 (MCA)	5.0	9.5	3.18	6.83	61.2	2.76

Furthermore, the g-C_3N_4 (MCA) sample exhibits the highest specific surface area, exceeding those of the other samples by more than a factor of two (Brunauer–Emmett–Teller (BET) analysis). This larger powder surface area may improve electrolyte access and contribute to the enhanced photoelectrochemical response, although electrode accessibility also depends on film structure. The samples were also characterized by diffuse reflectance spectroscopy. All samples absorb light in the visible range (Figure 1(b)). The band gaps estimated by Kubelka–Munk/Tauc analysis for an indirect allowed transition range from 2.60 to 2.76 eV (Table 1); the corresponding Tauc plots are provided in Figure S1.

Photoelectrodes on fluorine-doped tin oxide (FTO)-coated glass were fabricated using three suspension-based deposition techniques: drop-coating, dip-coating and spin-coating (a detailed description of the methods is provided in the Online Supplementary Materials).[18-20] All photoelectrochemical measurements were carried out in a three-electrode electrochemical cell under constant stirring. The configuration included the prepared photoelectrode as the working electrode, a platinum counter electrode and a silver/silver chloride (Ag/AgCl) reference electrode. A 0.5 M aqueous solution of Na_2SO_4 served as the electrolyte (Figure S2; details are provided in the Online Supplementary Materials). Illumination was provided by a 410 nm light-emitting diode (LED); the illuminated electrode area was 1 cm^2.

For spin-coating, the rotation speed, acceleration and duration were additionally optimized (Tables S1–S2). The selected parameters are summarized in Table 2. Under these conditions, the spin-coated electrode showed the highest photocurrent density (3.65 μA cm^{-2}), approximately twice as high as the values obtained for the other deposition methods (Figure 2(a)). Additional characterization of the films, including optical microscopy, mass loading measurements, double-layer capacitance analysis and electrochemical impedance spectroscopy (EIS), is provided in the Online Supplementary Materials (Figures S3–S6). Spin-coating gave the lowest mass loading and retained its advantage in a separate comparison at similar mass loadings. Together with the higher double-layer capacitance and lower impedance, these results suggest more effective charge transport in the spin-coated films. The lower loading may additionally favor charge collection by reducing optical shielding and shortening transport pathways.[21,22]

In the second stage, the optimized spin-coating procedure was kept unchanged to compare g-C_3N_4 samples from different precursors. According to the chronoamperometry data (Figure 2(b)), g-C_3N_4 (MCA) exhibits the highest photocurrent density under illumination, reaching 4.56 μA cm^{-2}, exceeding those of the g-C_3N_4 (M) and g-C_3N_4 (DCDA) photoelectrodes. Long-term measurements confirmed ~95% retention of the maximum photocurrent after 180 min (Figure S7). EIS was used to interpret the photoelectrochemical response and assess charge transport. The EIS spectra recorded under continuous 410 nm illumination at 0 V vs Ag/AgCl after a 10 min stabilization period (Figure 2(c)) show the lowest overall impedance for g-C_3N_4 (MCA), consistent with more favorable charge transport. The spectra were fitted using the equivalent circuit shown in Figure 2(d); detailed measurement conditions, a comparison with dark-state measurements and interpretation of the circuit are provided in the Online Supplementary Materials (Figure S8).

Table 2 Optimized parameters for the fabrication of g-C_3N_4 (DCDA) thin-film photoelectrodes. The optimal solvent, drying temperature and time for all three deposition methods were acetone, 50 °C and 1 h, respectively.

Deposition method	*Volume*/ml	*Mass*/mg	Number of layers	I_{ph}/μA·cm^{-2}
Dip-coating	5	5	3	1.54
Drop-coating	10	10	3	1.68
Spin-coating [a]	10	10	3	3.65

[a] Rotation speed 3000 rpm, acceleration 400 rpm·s^{-1}, duration 10 s.

The equivalent circuit comprises the series resistance R, two R–CPE circuits (CPE denotes a constant phase element) representing fast and slow relaxation processes and a Warburg element for diffusion-related impedance. The assignments were assessed using distribution of relaxation times (DRT) analysis (see the Online Supplementary Materials).

© Mendeleev Communications.

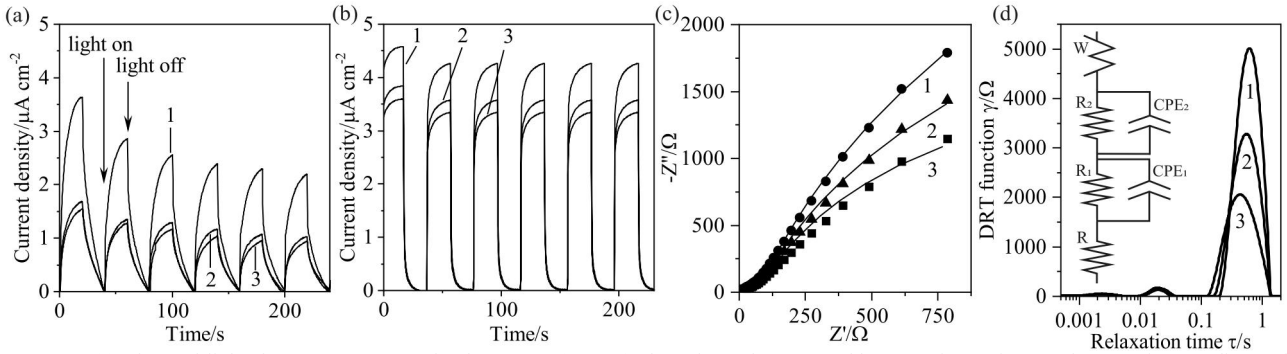


Figure 2 (a) Chopped-light chronoamperometry for the g-C_3N_4 (DCDA) photoelectrodes prepared by: 1 - spin-coating, 2 - drop-coating, 3 - dip-coating; (b) chopped-light chronoamperometry for: 1 - g-C_3N_4 (MCA), 2 - g-C_3N_4 (M), 3 - g-C_3N_4 (DCDA); (c) Nyquist impedance plots recorded under continuous 410 nm illumination at 0 V vs Ag/AgCl for: 1 - g-C_3N_4 (DCDA), 2 - g-C_3N_4 (M), 3 - g-C_3N_4 (MCA); lines show the corresponding fits; (d) distribution of relaxation times (DRT) curves: 1 - g-C_3N_4 (DCDA), 2 - g-C_3N_4 (M), 3 - g-C_3N_4 (MCA).

Table 3 Parameters obtained by fitting EIS data to an equivalent electrical circuit

Sample	R/Ω	R_1/Ω	p_{CPE_1}	T_{CPE_1}/Ω$^{-1}\cdot s^{p_{CPE_1}}$	R_2/Ω	p_{CPE_2}	T_{CPE_2}/Ω$^{-1}\cdot s^{p_{CPE_2}}$	R^2
g-C_3N_4 (DCDA)	2.45	98.3	0.676	235×10^{-6}	1.04×10^4	0.883	118×10^{-6}	0.999
g-C_3N_4 (M)	2.48	101	0.657	230×10^{-6}	5.82×10^3	0.880	142×10^{-6}	0.998
g-C_3N_4 (MCA)	2.58	106	0.650	210×10^{-6}	3.44×10^3	0.887	163×10^{-6}	0.995

The largest differences were observed for R_2 (Table 3), tentatively assigned to the slower charge-transport process in the particulate layer: g-C_3N_4 (MCA) showed the lowest value (3.44×10^3 Ω), approximately one-third of that for g-C_3N_4 (DCDA) (1.04×10^4 Ω), with g-C_3N_4 (M) showing an intermediate value (5.82×10^3 Ω). This lower R_2 is consistent with more favorable charge transport in the g-C_3N_4 (MCA) layer and may reflect its structural and textural characteristics.[10]

The DRT analysis (Figure 2(d)) suggests three relaxation regions: a fast feature at ~10^{-3} s corresponding to R_1-CPE_1, an intermediate ~10^{-2} s feature associated with the Warburg diffusion contribution and a dominant slower feature at 10^{-1}-10^0 s corresponding to R_2-CPE_2. Table S3 compares DRT features with fitted relaxation times. For g-C_3N_4 (MCA), the shift of the R_2-CPE_2 feature to shorter times, together with its lower R_2, suggests more favorable charge transport, consistent with its superior photoelectrochemical response.

Both photoelectrode fabrication and precursor-dependent synthesis conditions affect the photoelectrochemical performance of g-C_3N_4. Spin-coating provided the highest photocurrent density at the lowest mass loading, alongside higher double-layer capacitance and more favorable charge transport. The MCA-derived sample achieved 4.56 μA cm^{-2}, exceeding the photocurrent densities of melamine- and DCDA-derived samples. Measurements were performed at 0 V vs Ag/AgCl under 410 nm illumination. The photocurrent and area reported by Aidli et al. yield ~0.51 μA cm^{-2} for pristine g-C_3N_4 at 0 V vs Ag/AgCl under 395 nm illumination in 0.1 M sodium sulfate.[23] Differences in illumination and electrolyte concentration limit direct comparison. EIS/DRT analysis showed that R_2 for g-C_3N_4 (MCA) was approximately one-third of that for g-C_3N_4 (DCDA), with the corresponding relaxation feature shifted to shorter times. These trends are consistent with the distinct structural and textural characteristics of the g-C_3N_4 (MCA) sample and its enhanced photoelectrochemical response.

This work was supported by the Russian Science Foundation (grant no. 24-13-00416). The authors are grateful to E. A. Mel'gunova for the BET analysis. The XRD and BET investigations were performed using the facilities of the shared research center "National Center of Investigation of Catalysts" at Boreskov Institute of Catalysis.

Online Supplementary Materials

Supplementary data associated with this article can be found in the online version at doi: 10.71267/mencom.8137

References

1. A. V. Zhurenok, D. B. Vasilchenko and E. A. Kozlova, *Int. J. Mol. Sci.*, 2023, **24**, 346; https://doi.org/10.3390/ijms24010346.
2. J. Wen, J. Xie, X. Chen and X. Li, *Appl. Surf. Sci.*, 2017, **391**, 72; https://doi.org/10.1016/j.apsusc.2016.07.030.
3. M. I. Chebanenko, L. A. Lebedev, M. I. Tenevich, K. Eremeev, P. Loiko, A. Braud, V. P. Chelibanov, N. D. Prasolov and V. I. Popkov, *Int. J. Hydrogen Energy*, 2026, **246**, 155735; https://doi.org/10.1016/j.ijhydene.2026.155735.
4. E. Sdoukou, M. Antonopoulou, Z. Frontistis and I. Konstantinou, *J. Ind. Eng. Chem.*, 2026, **162**, 635; https://doi.org/10.1016/j.jiec.2026.05.018.
5. V. Yu. Yurova, K. O. Potapenko, T. A. Aliev, E. A. Kozlova and E. V. Skorb, *Int. J. Hydrogen Energy*, 2024, **81**, 193; https://doi.org/10.1016/j.ijhydene.2024.07.245.
6. J. Wei, W. Peng, W. Huang, W. Xu and W. Yang, *Microchem. J.*, 2026, **224**, 117766; https://doi.org/10.1016/j.microc.2026.117766.
7. O. V. Alekseeva, V. D. Shibaeva, A. V. Noskov and A. V. Agafonov, *Physica B*, 2026, **727**, 418302; https://doi.org/10.1016/j.physb.2026.418302.
8. A. V. Zhurenok, T. V. Larina, D. V. Markovskaya, S. V. Cherepanova, E. A. Mel'gunova and E. A. Kozlova, *Mendeleev Commun.*, 2021, **31**, 157; https://doi.org/10.1016/j.mencom.2021.03.004.
9. P. Xia, G. Li, X. Li, S. Yuan, K. Wang, D. Huang, Y. Ji, Y. Dong, X. Wu, L. Zhu, W. He and L. Qiao, *Crystals*, 2022, **12**, 1719; https://doi.org/10.3390/cryst12121719.
10. K. O. Potapenko, V. A. Lomakina, E. E. Aydakov, D. D. Mishchenko, D. V. Markovskaya, E. Y. Gerasimov and E. A. Kozlova, *J. Photochem. Photobiol. A*, 2026, **478**, 117207; https://doi.org/10.1016/j.jphotochem.2026.117207.
11. A. V. Zhurenok, K. O. Potapenko, D. V. Markovskaya, N. D. Sidorenko, S. V. Cherepanova, E. Y. Gerasimov, A. A. Saraev and E. A. Kozlova, *Int. J. Hydrogen Energy*, 2024, **51**, 1367; https://doi.org/10.1016/j.ijhydene.2023.09.195.

© Mendeleev Communications.

12. J. Safaei, N. A. Mohamed, M. F. M. Noh, M. F. Soh, M. A. Riza, N. S. M. Mustakim, N. A. Ludin, M. A. Ibrahim, W. N. R. W. Isahak and M. A. M. Teridi, *J. Alloys Compd.*, 2018, **769**, 130; https://doi.org/10.1016/j.jallcom.2018.07.337.
13. N. Sahu, B. Parija and S. Panigrahi, *Indian J. Phys.*, 2009, **83**, 493; https://doi.org/10.1007/s12648-009-0009-z.
14. M. Caux, F. Fina, J. T. S. Irvine, H. Idriss and R. Howe, *Catal. Today*, 2017, **287**, 182; https://doi.org/10.1016/j.cattod.2016.11.007.
15. N. N. Vu, C. C. Nguyen, S. Kaliaguine and T. O. Do, *ChemSusChem*, 2019, **12**, 291; https://doi.org/10.1002/cssc.201802394.
16. S. Sun, J. Li, P. Song, J. Cui, Q. Yang, X. Zheng, Z. Yang and S. Liang, *Appl. Surf. Sci.*, 2020, **500**, 143985; https://doi.org/10.1016/j.apsusc.2019.143985.
17. F. Fina, S. K. Callear, G. M. Carins and J. T. S. Irvine, *Chem. Mater.*, 2015, **27**, 2612; https://doi.org/10.1021/acs.chemmater.5b00411.
18. S. C. Ray, *Sol. Energy Mater. Sol. Cells*, 2001, **68**, 307; https://doi.org/10.1016/S0927-0248(00)00364-0.
19. A. A. M. Farag and I. S. Yahia, *Opt. Commun.*, 2010, **283**, 4310; https://doi.org/10.1016/j.optcom.2010.06.081.
20. T. Mahvelati-Shamsabadi and B. K. Lee, *Catal. Today*, 2020, **358**, 412; https://doi.org/10.1016/j.cattod.2020.08.005.
21. S. M. Thalluri, L. Bai, C. Lv, Z. Huang, X. Hu and L. Liu, *Adv. Sci.*, 2020, **7**, 1902102; https://doi.org/10.1002/advs.201902102.
22. M. G. Sendeku, T. A. Shifa, F. T. Dajan, K. B. Ibrahim, B. Wu, Y. Yang, E. Moretti, A. Vomiero and F. Wang, *Adv. Mater.*, 2024, **36**, 2308101; https://doi.org/10.1002/adma.202308101.
23. W. Aidli, D. Fumagalli, H. Helli, L. Falciola and V. Pifferi, *ChemElectroChem*, 2024, **11**, e202300557; https://doi.org/10.1002/celc.202300557.

Received: 3rd July 2026; Com. 26/8137

© Mendeleev Communications.